An Experimental Study of the Deformation Fields Around a Propagating Crack Tip

by Y. J. Chao, P. F. Luo and J. F. Kalthoff

ABSTRACT—Digital image processing was used to obtain the deformation fields around a propagating crack tip from photographic films recorded by a high-speed Cranz-Schardin camera. The in-plane displacements and strains determined from the process were then used to compute the dynamic stress intensity factor and the remote stress component parallel to the crack face. K dominance is discussed using the experimental data. Surface roughness of the fractured surface is also examined.

Introduction

In the past two decades, experimental studies of fracture dynamics and dynamic fracture parameters of engineering materials were performed by using, among others, caustic technique,[1,2] dynamic photoelasticity[2–4] and coherent gradient sensing.[5] Recently, an alternative approach using the in-plane displacement fields at a propagating crack tip for the determination of dynamic stress intensity factor (K_1^{dyn}) was employed. Arakawa *et al.*[6] and Sanford[7] used moiré interferometry to obtain the U and/or V displacement fields around propagating crack tips in Homalite-100 and 7075-T6 aluminum alloy plates. The dynamic stress intensity factor K_1^{dyn} was determined using the J contour integral or the theoretical asymptotic crack tip fields.

In 1985, Peters *et al.*[8] first employed the digital image correlation technique combined with high-speed photography to the study of a dynamic fracture problem. They obtained the deformation fields around a stationary crack as the specimen was loaded by impact. The transient $K_1^{dyn}(t)$ was then determined from the displacement fields. In this paper, we further extend the procedure to the study of crack propagation problems. An improved optical arrangement and an up-to-date image-processing method are used in the current paper so that more detailed crack tip information could be obtained. The images of the area surrounding a propagating crack tip in Araldite B were recorded by a Cranz-Schardin high-speed camera. The images on the photographic film were later digitized into a computer, and the digital correlation procedures were employed to obtain the displacement and strain fields. The dynamic stress intensity factors K_1^{dyn} and the remote stress component σ_{0x}^{dyn} were determined using a least squares fit of the experimentally determined displacements to the theoretical asymptotic crack tip fields. The K_1^{dyn} obtained compares well with the published results. The size and shape of the region surrounding the crack tip in which K_1^{dyn} dominance exists are evaluated. Crack opening profile is obtained and discussed relative to K_1^{dyn} dominance. Surface roughness distribution on the fractured surface was examined to correlate with the crack propagation speed.

Y. J. Chao (SEM Member) is Professor, Department of Mechanical Engineering, University of South Carolina, Columbia, SC 29208. P. F. Luo (SEM Member) is Associate Professor, Department of Mechanical Engineering, Chung Hua Polytechnique Institute, Hsin-Chu, Taiwan, R.O.C. J. F. Kalthoff is Professor, Institute for Experimental Mechanics, Ruhr University at Bochum, Germany.

Original manuscript submitted: July 28, 1997.
Final manuscript received: February 9, 1998.

Experiment

The experiments were carried out in a laboratory setting using a drop weight tower and an Instron loading machine. The imaging system for the tests is shown in Fig. 1. A Cranz-Schardin camera with 24 sparks and a maximum framing speed of 0.5 μs was used. Each spark acts like a point light source. A field lens behind the specimen collects the light passing through the specimen and converges the light to a point at plane B. A bellow-type photographic camera with 24 lenses placed at plane B focuses the specimen surface to the film plane. This arrangement keeps a relatively small distance between the specimen and the field lens so that the pseudo-Schlieren effect generated from the light passing through the high strain-gradient region at the crack tip is effectively reduced. As a consequence, the size of the dark spot at the crack tip recorded on the film is minimized. Hence, experimental data close to the crack tip can be retrieved from the recorded photographic film.

Three-point-bend specimen [SE(B)] was used in the tests. The geometry and dimensions are shown in Fig. 2. The transparent specimens of PMMA and Araldite B (properties given in Fig. 2) were spray painted with black paint on the surface facing the camera such that a speckle-like pattern was created. To record a detailed speckle pattern from the crack tip region, the area of interest (i.e., crack tip) of the specimen surface was magnified. To achieve this, the setup in Fig. 1 uses only 6 of the 24 frames of the camera and yields an overall magnification factor of 1.6× when imaged from the specimen surface to the film plane of the Cranz-Schardin camera.

A circular hole of 1.5 ϕ mm was drilled at the location of the crack tip when the specimen was made. This finite radius notch tip stores more energy at the tip than a sharp crack tip before the propagation event. Thus, a higher crack tip velocity can be achieved at the onset of crack propagation.

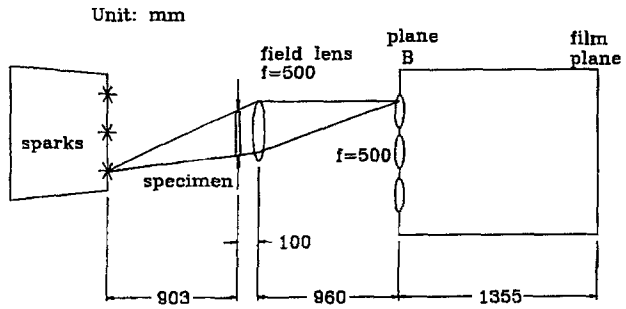

Fig. 1—Imaging system used in the test

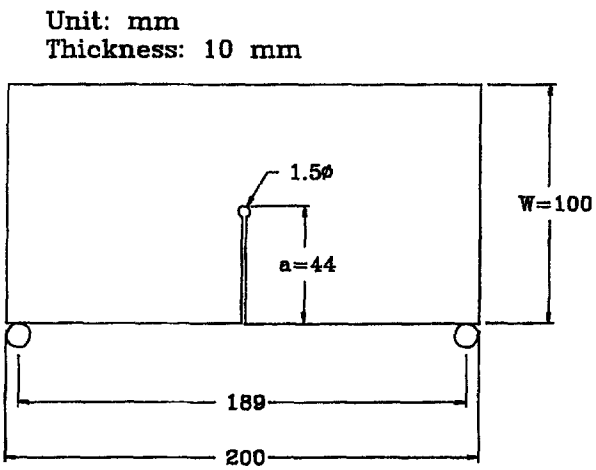

Fig. 2—Dimensions of the SE(B) specimen and material properties of Araldite B

However, in the first test, plastic deformation was observed around the loading point of the Araldite B specimen. It was decided to slightly cut the notch tip with a sharp knife before the test for the subsequent experiment.

Tests were performed using three types of loading: (1) static load (displacement controlled) from an Instron machine until the specimen broke, (2) impact load from a drop weight with a stationary crack and (3) impact load from a drop weight to break the specimen. In this paper, only the results from test (1) for an Araldite B specimen are presented. More results from (1), (2) and (3) for both PMMA and Araldite B specimens are being analyzed and will be reported later.

In test type (1), the sparks are triggered by interruption of a laser beam. The laser beam is arranged to pass through the specimen at a 45-deg angle to the specimen surface and perpendicular to the crack line. The laser beam passes through the midplane of the specimen at a location through which crack is expected to propagate. A photodiode is placed at the other side of the specimen to receive the laser beam. When the running crack tip passes the location where the laser beam is located, the new crack face reflects the laser light, and hence blocks the light beam to the photodiode. This interruption triggers the sparks, and consequently images of the specimen surface are recorded on the film.

The photographic films with images of propagating crack tip were later digitized into an IBM/AT computer using the Videk Megaplus digital camera (1024 × 1024 pixels) at the University of South Carolina (USC); 25 pixels/1 mm on the specimen surface was used when the photographic images were transferred into digital images. The digital correlation technique developed at USC[9–11] was then applied to analyze the digital images. The standard correlation procedure was used to obtain (1) the U and V displacement fields that are parallel and perpendicular to the crack line, respectively, and (2) the ε_x, ε_y, ε_{xy} strain fields after a smoothing process.

In what follows, a brief description of the digital image correlation method is first provided; the theoretical asymptotic crack tip fields are outlined next; and finally the experimental results are presented and discussed.

Digital Image Correlation Method

The digital image correlation method was first developed at USC in the early 1980s.[9–11] It is demonstrated that digital photographic images of deformed solids could be analyzed to estimate the in-plane displacements of various points on the surface. The analysis methodology employed the basic continuum mechanics theory of deformation to develop and implement a procedure for estimating surface displacements.

The experimental procedure starts by creating a random black-and-white dot pattern on the specimen surface, such as shown in Fig. 3. These patterns, one before and one after the load is applied, are then imaged by a digital camera and stored in a computer in a digital format. Note that this imaging process can be done directly from a specimen during the test or from a photographic film. In the current work, the random pattern was painted on the specimen surface and photographed onto the film using the Cranz-Schardin high-speed camera while the crack was propagating.

During the imaging process, the intensity of the random pattern is transformed into a finite number of samples on a rectangular grid. Each sensor, or pixel, in a typical CCD camera averages the incident light intensity to obtain a value, which is in the range of 0 to 255 for the intensity. To increase the accuracy of the correlation method, an interpolation scheme is used to reconstruct a continuous intensity surface instead of a discrete intensity pattern. A bilinear interpolation scheme is used in our current version of the software.

With the digitized images, before and after deformation, ready in the computer, the next step is to "match" digitally the subset from one image to another. For instance, let us choose a subset, say 10 × 10 pixels, from the undeformed image and try to find its location in the deformed image. Once the location of this subset in the deformed image is found,

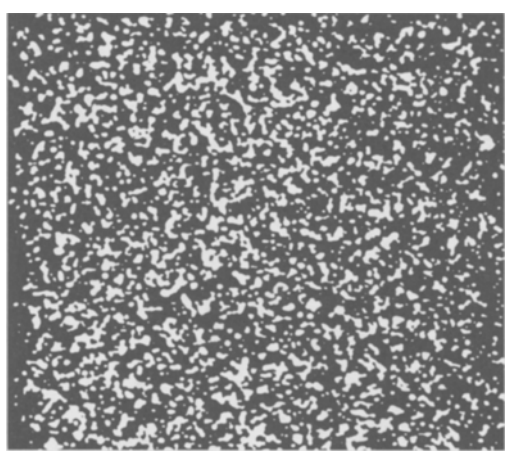

Fig. 3—A random black-and-white dot pattern to use with the digital correlation method

the displacement of this subset is known. This matching procedure is the correlation scheme, which is described in Fig. 4.

Figure 4 presents a graphical description of the basic concepts used to estimate the surface deformations of a deformable body using digitally recorded images. The small squares on the sampling grid represent the individual pixels in the camera's sensor plane, and (s, t) represent rectangular coordinates in the sensor plane.

First, consider a small subset S_u of the image of a planar object. The image is considered to be the undeformed image of the object and represents the initial position for the following analysis. In addition, the image is assumed to uniquely correspond to a subset on the object. In sensor plane coordinates, the intensities of the centerpoint P and any other point Q are written as

$$\begin{aligned} I(P) &= I(r, s) \\ I(Q) &= I(r + dr, s + ds), \end{aligned} \tag{1}$$

where (dr, ds) represent small distances in the (r, s) coordinate system. After deformation of the object, subset S_u is deformed into subset S_d, point P is deformed to point P^* and point Q is deformed to point Q^*. The positions of points P^* and Q^* are

$$\begin{aligned} I(P^*) &= (r + u(P), s + v(P)) \\ I(Q^*) &= \left(r + u + \frac{\partial u}{\partial r}dr + \frac{\partial u}{\partial s}ds, s + v \right. \\ &\quad \left. + \frac{\partial v}{\partial r}dr + \frac{\partial v}{\partial s}ds\right). \end{aligned} \tag{2}$$

If one assumes that the gradients are constant in the region, then each subset is assumed to be subjected to uniform strain. This assumption is manifested in Fig. 4 as a parallelogram shape for the deformed subset S_d. Thus, for each subset S_u that is chosen from the undeformed image, there are six parameters to determine: $u(P)$, $v(P)$ and the four partial derivatives. To obtain accurate estimates for these six variables, one first chooses a subset S_u from the undeformed intensity pattern. The subset S_u can be as small as 20×20 or as large as 50×50, depending on the size on the features in the intensity pattern.

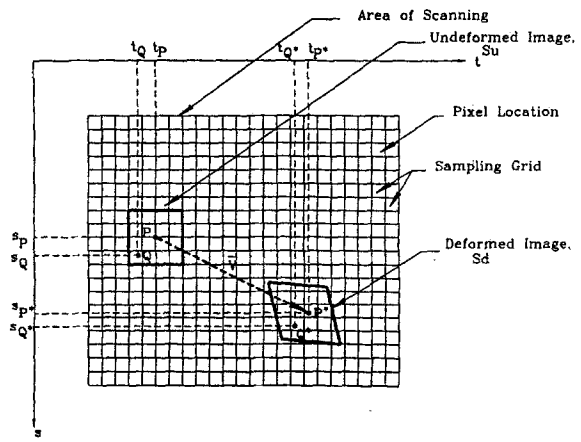

Fig. 4—A schematic of the deformed and undeformed subsets

Next, a range of values are chosen for the displacements $u_1(P)$ and $v_1(P)$, with the gradients set equal to zero. The intensity values in S_u are compared to an equal number of intensity values from the deformed image at locations $(r + u_1(P), s + v_1(P))$. To determine which is the best estimate for the displacements, a normalized cross-correlation coefficient is defined as

$$\begin{aligned} &C_1\left(u, v, \frac{\partial u}{\partial r}, \frac{\partial u}{\partial s}, \frac{\partial v}{\partial r}, \frac{\partial v}{\partial s}\right) \\ &= \frac{\sum_{i=1}^{N}\sum_{j=1}^{M} I_u(r_i, s_j) \cdot I_d(r_i + u_1, s_j + v_1)}{\sum_{i=1}^{N}\sum_{j=1}^{M}(I_u^2(r_i, s_j) \cdot I_d^2(r_i + u_1, s_j + v_1))^{1/2}}, \end{aligned} \tag{3}$$

where (u_1, v_1) take on all values within the range chosen for the displacement. The displacement $(u_1(P), v_1(P))$ which maximizes the correlation coefficient C_1 is assumed to represent the best estimates of the translation. Both Newton-Raphson and course-fine search methods have been used to optimally estimate the centerpoint displacement at each point while assuming zero gradients.

In practice, the choice of zero for the gradients of displacement does not appear to induce either bias or major random errors in the estimates of the centerpoint displacement $(u_1(P), v_1(P))$. After experimentation, it was found that the simplest option with reasonable accuracy is the use of subset translation with zero gradients and smoothing of the displacement data. The iteration process would proceed as follows. After computing the first estimate of centerpoint translation with zero gradients $(u_1(P), v_1(P))$, the search process varies both the gradients and displacements to maximize (3). The values of u, v and gradients that yield the maximum in (3) are the best estimates for the point P. Typical accuracy for this procedure is about ± 0.05 pixel.

By obtaining the displacements of many points P in the field, a displacement field is generated. The displacement field is then smoothed by one of many techniques available, and the gradients are estimated with improved accuracy. Typical accuracy of this approach is ± 150 μstrain in a nonuniform strain field.

Theoretical Background—Asymptotic Crack Tip Fields

The asymptotic crack tip fields under steady-state conditions are given as an infinite series by Nishioka and Atluri.[12] The displacement fields under Mode I condition can be written as

$$\begin{aligned} U &= \sum_{n=1}^{\infty} \frac{K_n B_I(C)}{2\mu}\sqrt{\frac{\pi}{2}}(n+1)\left\{r_1^{\frac{n}{2}}\cos\left(\frac{n\theta_1}{2}\right)\right. \\ &\quad \left. - h(n) r_2^{\frac{n}{2}}\cos\left(\frac{n\theta_2}{2}\right)\right\} \\ V &= \sum_{n=1}^{\infty} \frac{K_n B_I(C)}{2\mu}\sqrt{\frac{\pi}{2}}(n+1)\left\{-\beta_1 r_1^{\frac{n}{2}}\sin\left(\frac{n\theta_1}{2}\right)\right. \\ &\quad \left. + \frac{h(n)}{\beta_2} r_2^{\frac{n}{2}}\sin\left(\frac{n\theta_2}{2}\right)\right\}, \end{aligned} \tag{4}$$

where

$$C_l = \sqrt{\frac{(\kappa+1)\mu}{(\kappa-1)\rho}} \quad C_t = \sqrt{\frac{\mu}{\rho}}$$

$$\beta_1 = \sqrt{1-\left(\frac{C}{C_l}\right)^2} \quad \beta_2 = \sqrt{1-\left(\frac{C}{C_t}\right)^2}$$

$$\theta_m = \tan^{-1}\frac{\beta_m y}{x} \quad r_m = \sqrt{x^2+\beta_m^2 y^2} \quad m = 1, 2$$

$$h(n) = \frac{2\beta_1\beta_2}{1+\beta_2^2} \text{ for odd } n \quad h(n) = \frac{1+\beta_2^2}{2} \text{ for even } n$$

$$B_I(C) = \frac{1+\beta_2^2}{D}, \quad D = 4\beta_1\beta_2 - (1+\beta_2^2)^2.$$

Note that C is the speed of the propagating crack tip, $\kappa = (3-\nu)/(1+\nu)$ is for the plane stress conditions, ν is Poisson's ratio, μ is the shear modulus of elasticity and ρ is the density. In the series solution, the coefficient of the first (singular) term K_1 is equal to K_1^{dyn}, and the coefficient of the second term is related to the remote stress component σ_{0x}^{dyn} by $\sigma_{0x}^{dyn} = 3K_2\sqrt{\frac{2}{\pi}}$. Note that K_1^{dyn} is related to the dynamic energy release rate of the propagating crack tip and σ_{0x}^{dyn} is a parameter controlling crack curving and branching.[3,13]

The experimentally determined displacement data can be written as

$$U = \sum_{n=1}^{m} K_n f_n - \theta_u y + t_u$$
$$V = \sum_{n=1}^{m} K_n g_n + \theta_v x + t_v, \tag{5}$$

where $f_n = f_n(r_1, \theta_1, r_2, \theta_2)$ and $g_n = g_n(r_1, \theta_1, r_2, \theta_2)$ are known functions from eq (4) and $K_n, \theta_u, \theta_v, t_u$ and t_v are unknown coefficients to be determined. Note that θ_u, θ_v, t_u and t_v are included to eliminate any possible rigid body rotation and translation presented in the displacement data determined from the digital image correlation. Using a standard numerical procedure for the least squares fit[14] [i.e., using p data points with $n = 1, 2, \ldots, m$ terms in eq (5), where $p \geq (m+2)$], the coefficients $K_n, \theta_u, \theta_v, t_u$ and t_v in eq (5) can be determined. From K_1 and K_2, the dynamic fracture parameters K_1^{dyn} and σ_{0x}^{dyn} can then be determined.

Results

Figure 5 shows a set of photographs obtained from one particular test. Note that although 24 sparks are available, only six frames were recorded in all tests to accommodate the optical arrangement as discussed previously. The framing rate is 8 μs between any two successive frames. The dark spot on the right hand side of the crack is the area on the specimen surface without the random speckles to allow the laser light to pass through for triggering purpose. The instantaneous crack tip location in each frame is identified with an arrow. Note that the dark spot at the crack tip due to the pseudo-Schlieren effect is very small. The size of the dark spot recorded is approximately 1.5 mm in diameter on the film,

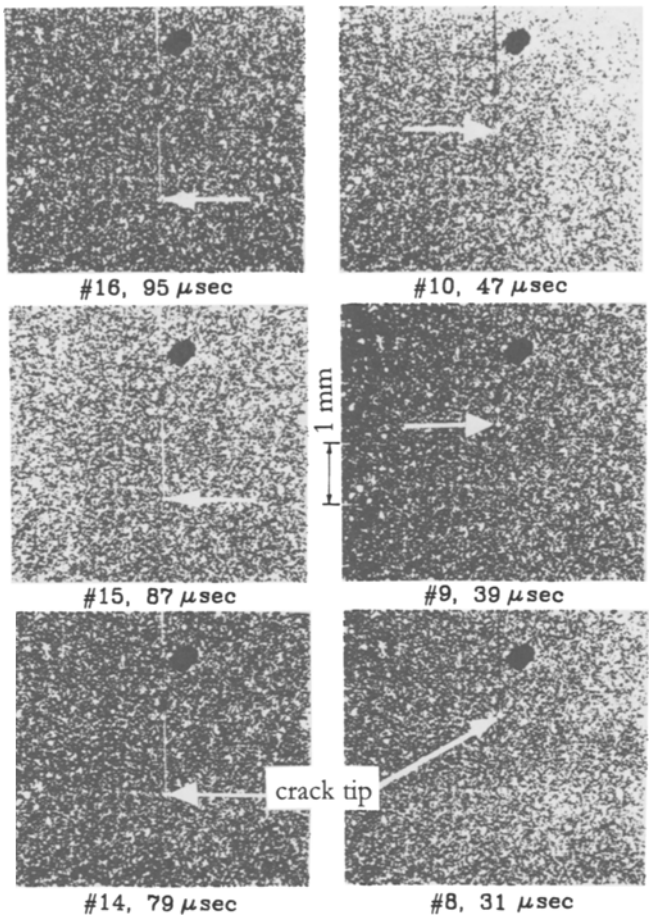

Fig. 5—A set of recorded pictures: Araldite B, SE(B), $a/W = 0.44$, specimen 4

which corresponds to about 1 mm on the specimen surface. Considering that the thickness of the test specimen is 10 mm, this dark spot is very small.

The crack tip speed is determined using locations of the crack tip on the recorded film. Figure 6 summarizes the measured results. For the pictures shown in Fig. 5, frames 14, 15 and 16 give an average crack tip speed of $C = 189.4$ m/s and frames 8, 9 and 10 give a speed of 303.4 m/s. The results reported in the following sections are from frame 15.

Figure 7 shows the U and V displacement fields, and Fig. 8 shows the strain fields around the propagating crack tip. The experimentally determined displacement data were then used with the procedure outlined in the previous section [i.e., eq (5)] for the determination of the dynamic stress intensity factor K_1^{dyn} and the remote stress component σ_{0x}^{dyn}. A total of 1540 displacement data from the region surrounded by the dashed line shown in Fig. 7 were used for the least squares fit. Results from a convergence study are presented in Fig. 9. A converged solution can be obtained when more than 12 terms in eq (4) are used. The final converged values are $K_1^{dyn} = 0.641$ MN/m$^{3/2}$, and $\sigma_{0x}^{dyn} = -4.1$ MPa. This $K_1^{dyn} = 0.641$ MN/m$^{3/2}$ is plotted in Fig. 10 to compare with the published data for Araldite B determined by caustic technique.[1] The current K_1^{dyn} value is less than the previous results. The second stress term, σ_{0x}^{dyn}, determined as -4.1 MPa in this test, indicates that the crack will propagate in a straight manner with no curving, since σ_{0x}^{dyn} is less than zero.[3,13]

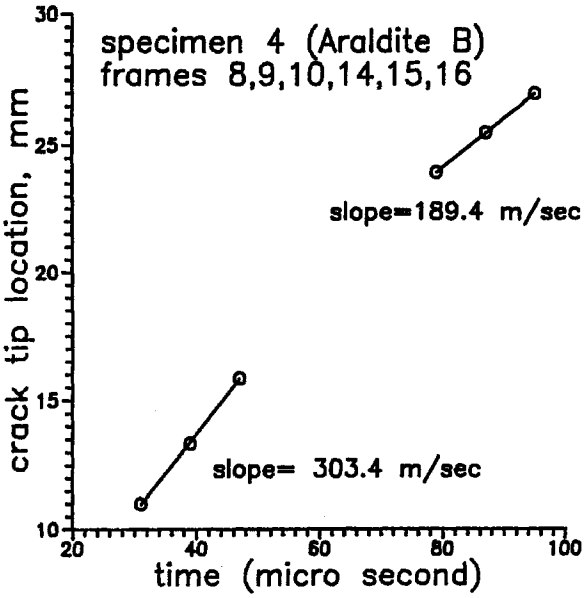

Fig. 6—Crack tip speed determination

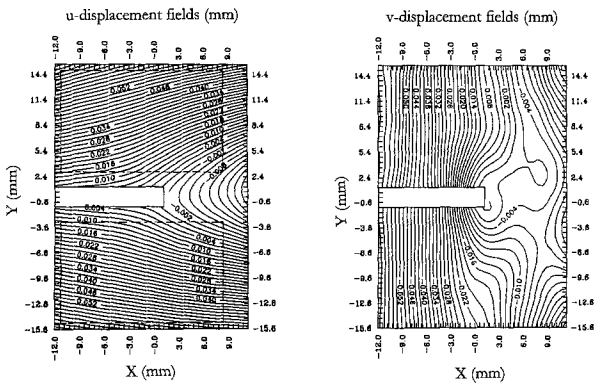

Fig. 7—U and V displacement fields: specimen 4, frame 15

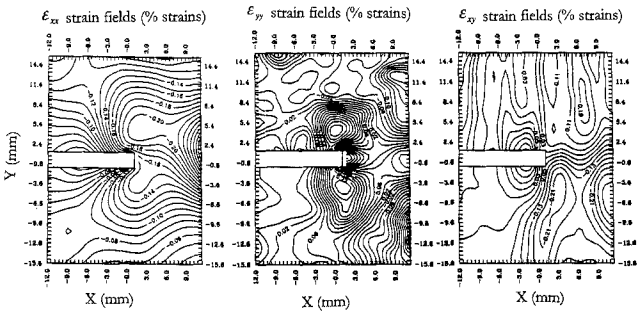

Fig. 8—Strain fields ε_x, ε_y and ε_{xy}: specimen 4, frame 15

Using the experimentally determined $K_1^{dyn} = 0.641$ MN/m$^{3/2}$, we evaluated the K_1^{dyn}-dominated zone using the U and V displacement fields. The K_1^{dyn}-dominated zone is defined as the region around the crack tip where the difference between the displacements determined by the leading term in eq (4) and the corresponding displacements determined experimentally is within an arbitrarily specified percentage. Figure 11 shows the results for 10 percent and 15 percent differences. It is interesting to note from Fig. 11 that the K_1^{dyn}-dominated zone determined by the U displacements has a butterfly shape and is leaning toward the front. On the other hand, a kidney shape of K_1^{dyn}-dominated zone is found for V displacement, and it is leaning toward the back relative to the direction of the crack propagation.

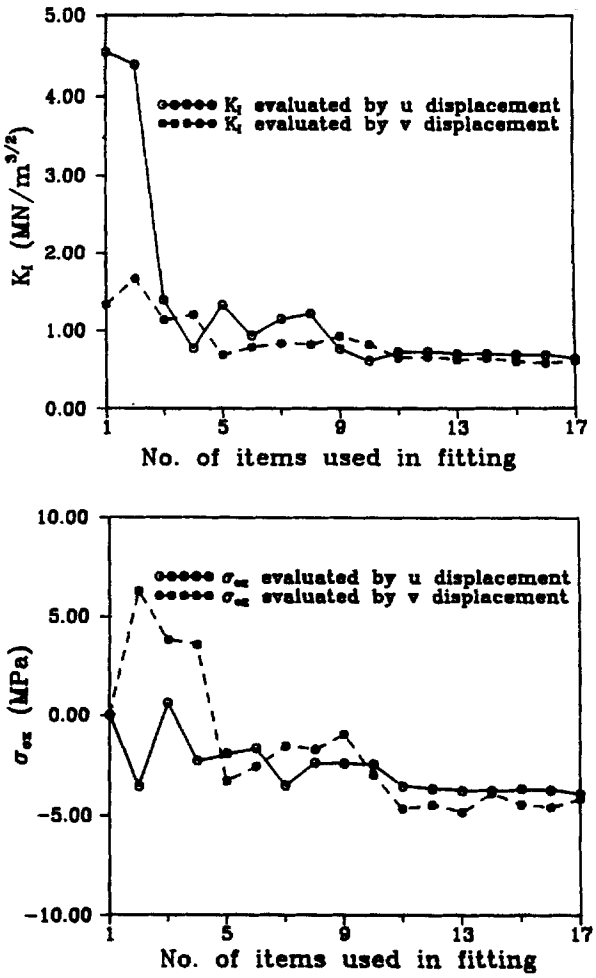

Fig. 9—Convergence study: specimen 4, frame 15

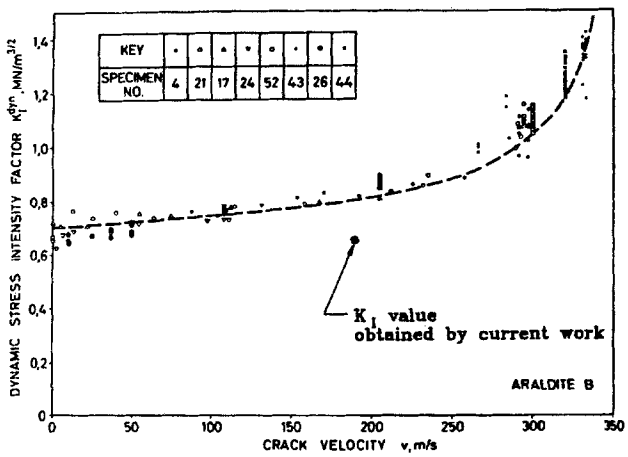

Fig. 10—K_1^{dyn} compared to published results (see Ref. 11)

The crack-opening profile (COP) is plotted in Fig. 12. Figure 12 shows that the V displacement along the crack face (i.e., $\theta = 180$ deg) matches well with the asymptotic solution eq (4) if 17 terms are used. The K_1^{dyn}-dominated zone evaluated using COP is less than 2 mm. These results also suggest that the crack tip opening displacements can be a

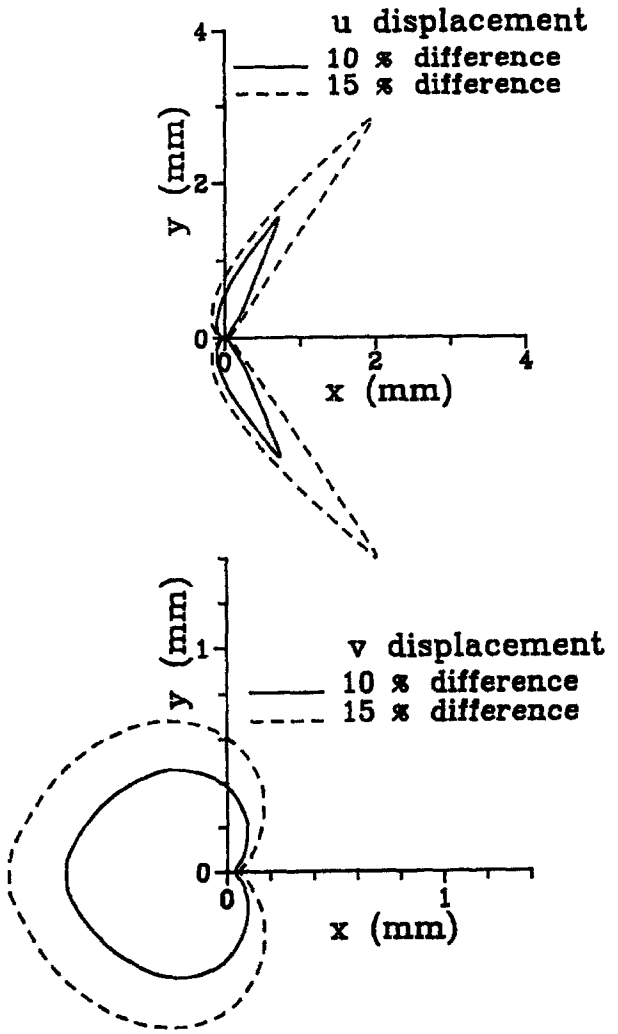

Fig. 11—K_1^{dyn}-dominated zone determined by U and V displacement fields

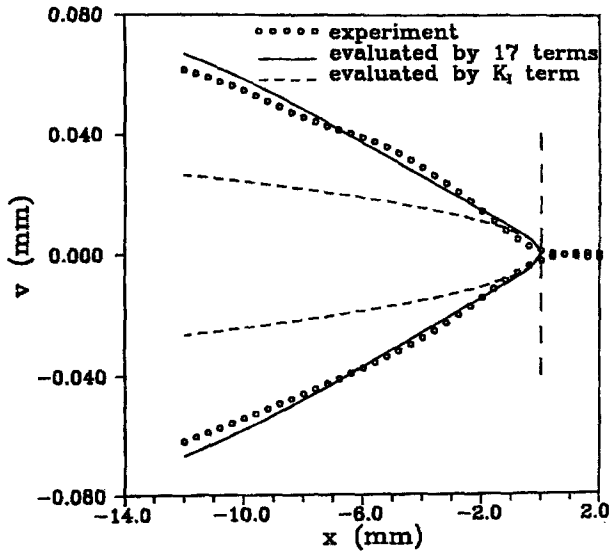

Fig. 12—Crack opening profile

By carefully examining the fractured surface, a decreasing surface roughness as the crack propagated is observed. The surface roughness of the fractured surface of specimen 4 was measured using a stylus apparatus having 0.01 μm resolution. Five measurements were taken at each position along the centerline of the fractured surface. Twenty-eight positions, 2 mm apart for any two adjacent positions, were used. The results are shown in Fig. 14. Figure 14 shows a decreasing surface roughness in the direction of the crack propagation, which correlates to a decreasing crack tip speed. Figure 14 indicates a rapid decrease of the crack tip speed in the initial phase of the crack propagation. With only two speeds available in this test as shown in Fig. 6, a quantitative relation between the propagation speed and surface roughness cannot be established. More good candidate for the determination of K_1^{dyn} when combined with eq (4).

Discussion

The error or noise associated with the digital correlation technique has been studied extensively and is generally accepted as ±0.05 pixels. With a magnification factor of 25 pixels/1 mm used in this report, the error is about 2.0 μm. The total noise level of the results is expected to be around 3 μm considering the additional possible errors from the transfer of images from photographic film to digital. Examining the magnitude of the test data shown in Fig. 7, it appears that most data obtained are outside this noise level.

The frame 15 in Fig. 5 has had a crack growth $\Delta a \sim$ 38 mm and a remaining ligament of 18 mm. At this location of the crack tip, the stress wave fronts released from the crack propagation initiation and reflected from the boundary have reached and passed the crack tip several times. However, the fractured surface does not appear to have the intermittent run-arrest traces. It appears that the effect from the reflected waves is small. Figure 13 shows a photograph of the fractured surface. In general, the fractured surface is fairly smooth with some river marks indicating a fast brittle fracture.

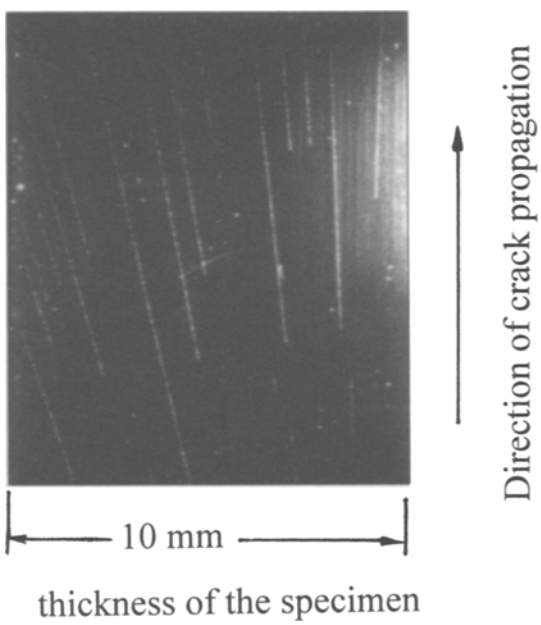

Fig. 13—Fractured surface showing the river marks

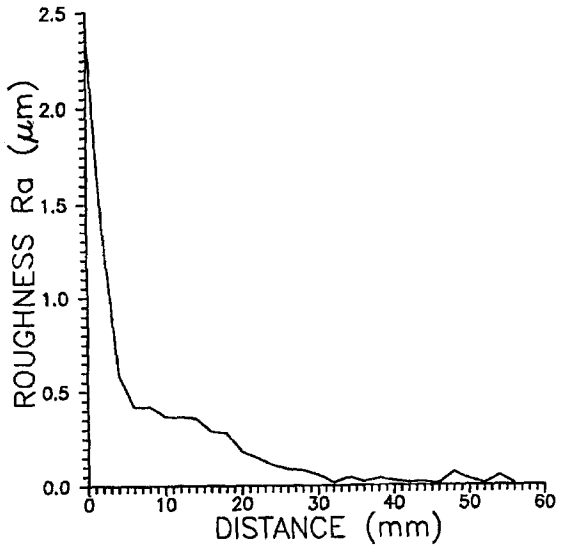

Fig. 14—Surface roughness distribution along the fractured surface (distance measured from the crack tip)

tests could be used to obtain this correlation, and the history of the crack propagation speed can be determined from the surface roughness of the fractured surface.

Note that a steady-state assumption (e.g., constant crack tip velocity) is used in the theoretical derivation of eq (4). Recent work by Freund and Rosakis[15] has shown that under certain conditions, the transient effect is important. Using the two crack tip speeds obtained in Fig. 6 and assuming a linear relation between the two groups of frames, there appears to exist a deceleration $\dot{v} = -2.38 \times 10^6$ m/s^2 = (303.4 − 189.4) (m/s)/48 μs to the crack tip. However, the deceleration should be large just around the initiation time and not so significant around frame 15, that is, not a linear relation with time. The effect of this deceleration to the crack tip fields reported in the current paper is not clear. More carefully designed experiments are needed to investigate this effect.

A direct conclusion from the results shown in this paper is that the digital image correlation technique combined with high-speed photography can be effectively used for the study of fracture dynamics. Further studies using the current experimental arrangement under transient conditions should be valuable in the understanding of crack initiation and arrest behavior of structural materials.

Acknowledgments

The experimental work was performed at the Institute for Experimental Mechanics, Ruhr University at Bochum, Germany, while the first author, Y. J. Chao, was on sabbatical leave from the University of South Carolina. A research fellowship granted to Y. J. Chao from the Alexander von Humboldt Foundation of Germany is greatly appreciated. In addition, Y. J. Chao wishes to thank all the graduate students and staff at the Institute for Experimental Mechanics, Ruhr University at Bochum, for their constant assistance during his stay. Particular thanks is due to Shinichiro Takahashi, Tokyo Institute of Technology, for his assistance in running the test. In addition, the support from the National Science Foundation through NSF/EPSCoR Cooperative Agreement No. EPS-9630167 is greatly appreciated. Finally, we are indebted to Professor Michael A. Sutton at the University of South Carolina for many helpful discussions related to the digital image processing technique.

References

1. Kalthoff, J.F., "Shadow Optical Method of Caustics," Handbook on Experimental Mechanics, Ch. 9, ed. A.S. Kobayashi, Prentice Hall, Englewood Cliffs, NJ (1987).

2. Nigam, H. and Shukla, A., "Comparison of the Techniques of Caustics and Photoelasticity as Applied to Fracture," EXPERIMENTAL MECHANICS, **28** *(2), 123–131 (1988).*

3. Ramulu, M., Kobayashi, A.S., and Kang, B.S.J., "Dynamic Crack Curving—A Photoelastic Evaluation," EXPERIMENTAL MECHANICS, **23** *(1), 1–9 (1983).*

4. Ramulu, M., Kobayashi, A.S., and Kang, B.S.J., "Dynamic Crack Branching—A Photoelastic Evaluation," Fracture Mechanic: 15th Symposium, ed. R.J. Sanford, ASTM STP 833, 130–148 (1984).

5. Krishnaswamy, S., Tippur, H.V., and Rosakis, A.J., "Measurement of Transient Crack Tip Deformation Fields Using the Method of Coherent Gradient Sensing," J. Mech. Physics Solids, **40** *(2), 339 (1992).*

6. Arakawa, K., Drinnon, R.H., Jr., Kosai, M., and Kobayashi, A.S., "Dynamic Fracture Analysis by Moiré Interferometry," EXPERIMENTAL MECHANICS, **31** *(4), 306–309 (1991).*

7. Sanford, R.J., "A Moiré Study of Dynamic Crack Propagation in Aluminum," Proc. SEM Spring Meeting, 344–349 (1991).

8. Peters, W.H., Ranson, W.F., Kalthoff, J.F., and Winkler, S.R., "A Study of Dynamic Near-crack-tip Fracture Parameters by Digital Image Analysis," J. Physique, colloque C5, 631–638 (1985).

9. Chu, T.C., Ranson, W.F., Sutton, M.A., and Peters, W.H., "Applications of Digital Image Correlation Techniques to Experimental Mechanics," EXPERIMENTAL MECHANICS, **25** *(3), 232–245 (1985).*

10. Sutton, M.A., Turner, J.L., Bruck, H.A., and Chae, T., "Full Field Representation of Discretely Sampled Surface Deformation for Displacement and Strain Analysis," EXPERIMENTAL MECHANICS, **31** *(2), 168–177 (1991).*

11. Chao, Y.J. and Sutton, M.A., "Accurate Measurement of Two and Three-dimensional Surface Deformations for Fracture Specimens by Computer Vision," Experimental Techniques in Fracture, Vol. 3, ed. J.S. Epstein, Society for Experimental Mechanics (1993).

12. Nishioka, T. and Atluri, S.N., "Path-independent Integrals, Energy Release Rate, and General Solution of Near-tip Fields in Mixed-mode Dynamic Fracture," Eng. Fract. Mech., **18** *(1), 1–22 (1983).*

13. Ramulu, M. and Kobayashi, A.S. "Mechanics of Crack Curving and Branching—A Dynamic Fracture Analysis," Int. J. Fract., **27**, *187–201 (1985).*

14. IMSL Subroutine, OFIMA3, Problem Solving Software System for Mathematical and Statistical Fortran Programming, Edition 9.2 (1984).

15. Freund, L.B. and Rosakis, A.J., "The Structure of the Near Tip Field During Transient Elastodynamic Crack Growth," J. Mech. Phys. Solids, **40** *(3), 699–719 (1992).*